Materials Today Energy 18 (2020) 100528

Contents lists available at ScienceDirect

Materials Today Energy

journal homepage: www.journals.elsevier.com/materials-today-energy/

Gradient electrodeposition enables high-throughput fabrication and screening of alloy anodes for high-energy lithium-ion batteries

C. Zhong [a, b, e], C. Guo [a, e], X. Jin [a], Y. Li [a], J. Chen [a], S. Zhang [a], Y. Lu [c], H. Zhang [a, d, *], F. Pan [b, **]

[a] National Laboratory of Solid State Microstructures, Collaborative Innovation Center of Advanced Microstructures, and College of Engineering and Applied Sciences, Nanjing University, 210093, Nanjing, China
[b] School of Advanced Materials, Shenzhen Graduate School, Peking University, Shenzhen, 518055, China
[c] School of Chemistry, Biology and Materials Engineering Suzhou University of Science and Technology, Suzhou, 215009, China
[d] Key Laboratory of Advanced Energy Materials Chemistry (Ministry of Education) Nankai University, Tianjin, 300071, China

ARTICLE INFO

Article history:
Received 29 June 2020
Received in revised form
15 August 2020
Accepted 17 August 2020
Available online 6 September 2020

Keywords:
Lithium-ion batteries
Gradient electrodeposition
High-throughput fabrication
Screening
Sn–Co–Sb alloy anode

ABSTRACT

Alloy anodes provide high capacity for high-energy lithium-ion batteries. Multi-element alloys require high-throughput fabrication technologies to facilitate the screening of alloy composition, morphologies, and structures. Here, we report a gradient electrodeposition method to prepare Sn–Co–Sb alloy anodes with varied Sn:Co:Sb ratios and demonstrate the effectiveness of gradient electrodeposition on alloy anode development. Using this technology, we can vary each metal element to form a gradient distribution in one direction by tilting the sample alternatively during each electrodeposition. Such gradient electrodeposition realizes the complex composition of Sn–Co–Sb alloys in one large sample, enabling high-throughput fabrication simultaneously. After annealing, the obtained Sn–Co–Sb alloy forms varied phases such as Sn, SnSb, and $CoSn_2$. It is noted that the elemental ratio has a significant influence on the microstructures and electrochemical performances of the deposited Sn–Co–Sb alloy. The Sn–Co–Sb alloy with a ratio of 71.3:12.8:15.9 delivers a high reversible capacity of 671.8 mAh g^{-1} and simultaneously shows excellent cyclability, which can be attributed to the optimal morphology structure and Sn:Co:Sb ratio. The optimized alloy can maintain a high capacity without sacrificing cyclability, which was usually limited by strain accumulation caused by high capacity. This work reports a general gradient electrodeposition technology for high-throughput screening of alloy anodes, which can also be applied to other alloy applications.

1. Introduction

Electrochemical energy storage devices play an imperative role in everyday lives. Lithium-ion (Li-ion) batteries are currently considered one of the promising technologies for electric vehicles and smart grid because of their high energy densities, excellent cycle performance, and environmental friendliness [1–3]. To meet the growing demand for energy density, the rapid development of anode materials with higher theoretical capacity, power, and energy density is urgently needed as the commercial graphite anode delivers relatively low theoretical capacity (372 mAh g^{-1}) [4–6]. In the past few decades, a large number of anode materials have been developed, including carbonaceous materials, alloy, metal oxides, metal sulfides, and metal carbides [7–10]. Among these materials, tin has aroused renewed interest as anode materials for Li-ion batteries because of its high theoretical capacity (around 991 mAh g^{-1}). However, there remains a problem as regards the capacity decay with cycling because of the large volume changes (about 300%) during charge and discharge [11].

If the severe volume change is not well managed, the accumulated stress often causes electrode disintegration and rapid capacity fading [12,13]. In recent years, considerable effort has been made to overcome stress-related problems by using nanostructured electrodes, porous scaffolds, composite materials, and so on [14–16].

* Corresponding author. National Laboratory of Solid State Microstructures, Collaborative Innovation Center of Advanced Microstructures, and College of Engineering and Applied Sciences, Nanjing University, 210093, Nanjing, China.
** Corresponding author.
E-mail addresses: hgzhang@nju.edu.cn (H. Zhang), panfeng@pkusz.edu.cn (F. Pan).
[e] These authors contributed equally to this work.

https://doi.org/10.1016/j.mtener.2020.100528
2468-6069/

Among these technologies, making Sn a composite is probably the most scalable approach to be integrated into the current battery industries. Many reports have discussed the role of a second element/phase to improve the cycle performance of Sn-based alloys [17,18]. An inactive phase can be added to serve as the buffer that partly alleviates the mechanical stress caused by the volume change of the active phase. Various Sn-M intermetallic compounds have been reported, such as Sn−Sb, Sn−Ni, Sn−Sb−Cu, Sn−Sb−Ni, and Sn−Co−Ni, and so on [11,19−22]. Sengupta et al. [22] electrodeposited dendritic ternary alloy using active/inactive composite to form 3D interconnect nickel foam. The multiphase composite of active and inactive intermetallics dispersed in the Sn matrix can alleviate the volumetric stress generated during cycling [22]. Zhang et al. [23] reported an electrodeposited Sn−Ni alloy on the porous Ni scaffold, which exhibits high rate properties because the alloy composite can buffer Li insertion and extraction of the binary tin-based anode. These studies have pushed forward the development of the alloy anode and received modest progress. However, such a study approach requires fabrication and characterization in each composition. For multiple elements, scattered or random sampling in the composition space would limit rapid optimization of alloy anodes. Therefore, a high-throughput fabrication and screening method is urgently needed to accelerate the development of multi-element alloy anodes.

Herein, we report a gradient electrodeposition method to prepare a series of Sn−Co−Sb alloy electrodes with varied ratios of Sn, Co, and Sb in one fabrication, as shown in Fig. 1. The high-throughput fabrication was realized by tilting and rotating the working electrode during each electrodeposition to attain a gradient distribution of each element. After annealing the multi-elemental gradients, the varied alloy composition was obtained in one large sample. The Sn−Sb−Co alloy electrode is evenly divided into 81 samples for characterization. Among the varied composition, the Sn−Co−Sb alloy with the mass ratio of 71.3:12.8:15.9 exhibits the high reversible capacity of 671.8 mAh g^{-1} and the significantly enhanced capacity retention during cycling. The excellent electrochemical properties can be attributed to the optimal Sn:Co:Sb ratio and morphologic structure. In general, we demonstrated a new strategy of the gradient electrodeposition method to quickly screen out the alloy anode for Li-ion batteries, and such a high-throughput screening technology could be applied to other alloy systems.

2. Results and discussion

The high-throughput fabrication (as shown in Fig. 1) differs from the conventional two-electrode electrodeposition. The working electrode was tilted to vary the diffusion distance between working and counter electrodes. Because the current density at the near edge of the sample is higher than that at the far edge, the mass of deposit varies along the tilting direction. In a conventional cell, both working and counter electrodes are in parallel, whereby metals are uniformly plated on the surface of a working electrode. In contrast, tilting electrodeposition enables a gradient distribution of alloy components (Fig. 1a). To deposit multi-element alloy, the sample was rotated after each deposition (Fig. 1b).

Four steps were adopted to form Sn−Co−Sb alloy. Ni foil was used as the working and counter electrodes. First, an Sn layer was electrodeposited from a tin chloride−containing plating solution. Second, the as-obtained sample (Ni@Sn) was rotated 90° and plated with Co in a Co^{2+}-containing solution. Third, Sb was electrodeposited onto the obtained Ni@SnCo after a 90° rotation. Fourth, the second layer of Sn was electrodeposited on the Ni@SnCoSb after the final 90° rotation. The resulting alloy sample was annealed at 300 °C for 2 h in Ar gas for further characterization.

A typical sample as shown in Fig. 2a was cut into 9 × 9 square samples (labeled as S01−S81). Each sample represents a different composition of Sn, Co, and Sb. To determine how the composition and morphological structure affect the electrochemical properties of the Sn−Co−Sb alloy, we present the analyses of nine samples (S01, S05, S09, S37, S41, S45, S73, S77, and S81 alloys) in Fig. 2b. The X-ray diffraction (XRD) patterns of nine Sn−Co−Sb alloy samples show the strong diffraction peaks around 44.5°, 51.9°, and 76.4°, which can be indexed to the Ni flat substrate (JCPDS card no. 65-2865) [24]. The hexagonal SnSb phase shows XRD peaks at 29.1°, 41.5°, and 41.8° (JCPDS card no. 33-0118) [22]. The peak at 35.5° is attributed to the $CoSn_2$ alloy component (JCPDS card no. 25-0256) [25]. Sn presents a characteristic peak of around 30.6° (JCPDS card no. 04-0673) [22]. The XRD patterns demonstrate that all these nine samples are mainly composed of phases of SnSb and $CoSn_2$ (with varied ratios). A metallic Sn phase appears in S05, S09, and S45 alloys.

Fig. 2c presents the scanning electron microscopy (SEM) images of these alloy samples. The S05 and S09 alloys exhibit relatively flat surface morphology, and no obvious porous structures are not observed. The S01, S37, S41, and S45 alloys show a 3D interconnected porous structure. The open porous microstructure provides a high surface area, which is favorable to enhance electrochemical properties because of better contact between the electrode and electrolyte and faster ion/electron transfer at interfaces. The S73, S77, and S81 alloys exhibit a large amount of small 1- to 3-μm particles on their surfaces. Thus, the SEM analyses show that the gradient electrodeposition can not only vary the

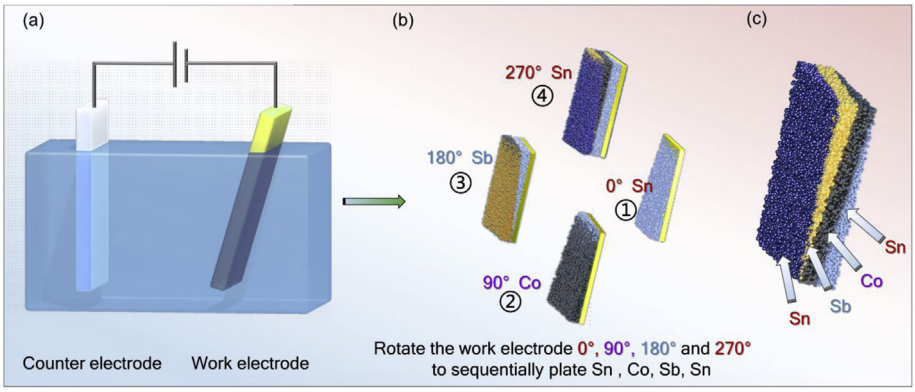

Fig. 1. Schematic illustration of the high-throughput fabrication of Sn−Co−Sb alloy *via* a gradient electrodeposition process: (a) Schematic diagram of the electrodeposition system with a tilting working electrode. (b) Sn, Co, Sb, and Sn were sequentially plated on the tilted sample after rotating. (c) Illustration of the gradient distribution of the electrodeposited Sn, Co, Sb, and Sn layers.

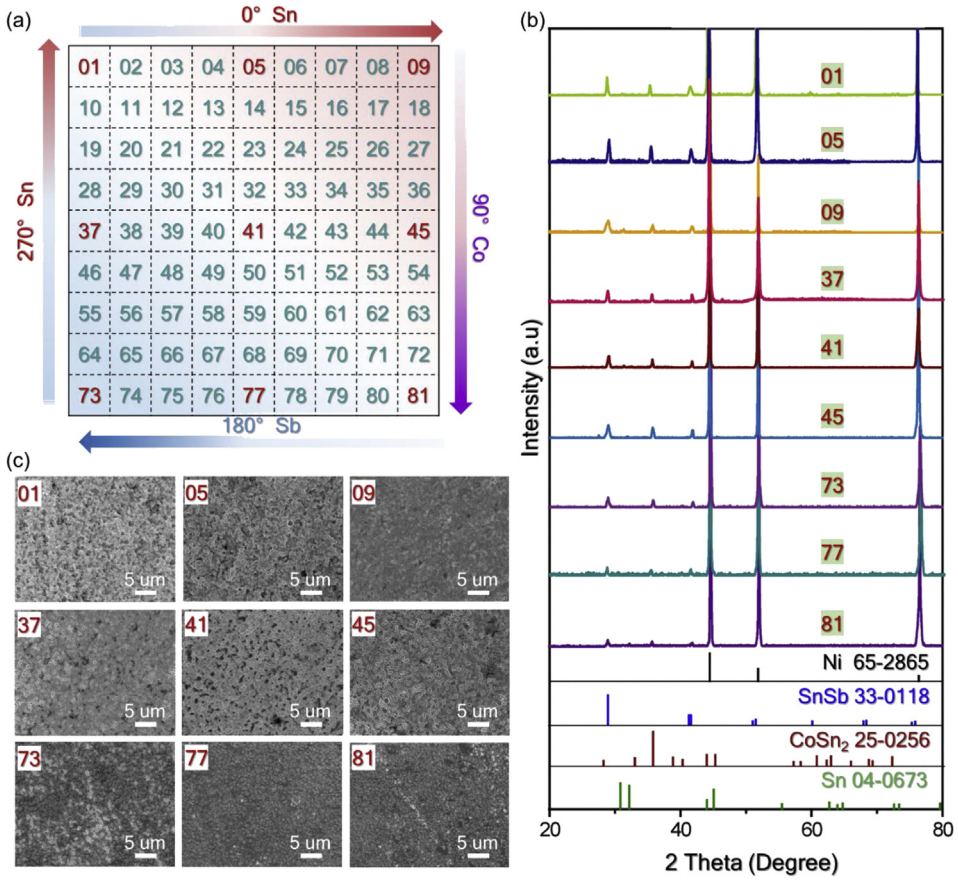

Fig. 2. (a) Plating direction and the sample number after the deposited alloy was cut into 91 small samples. (b) XRD patterns and (c) SEM images of selected alloy samples. XRD, X-ray diffraction; SEM, scanning electron microscopy.

composition but also change the alloy morphology, which affects the electrochemical properties of the alloy samples.

The elemental distribution and composition were analyzed by energy-dispersive X-ray (EDX) mapping and spectrum. The elemental mapping image of the S41 alloy in Fig. 3a indicates that Sn, Co, and Sb are uniformly distributed on the electrode. The relative mass ratios of elements were analyzed as per the EDX spectra (Fig. 3b). Fig. 3c summarizes the contents of Sn, Co, and Sb in nine alloy samples. The continuous composition change indicates that Sn, Co, and Sb can be finely varied in 9 × 9 samples at different positions. As illustrated in Fig. 3d, S09, S41, and S73 show a gradually decreased Sn content and increased Co:Sb ratios along the diagonal direction of the whole Sn–Co–Sb alloy. The change in Sn:Co:Sb ratios leads to the varied phase compositions in the different regions of the alloy sample. For example, high content of Sn in S09 renders extra Sn existing in the metallic phase. Thus, S09 has three phases of SnSb, $CoSn_2$, and Sn. With the further decrease in Sn and the increase in Co and Sb content, there are only SnSb and $CoSn_2$ phases in S73. Such a varied phase composition is realized in only one sample *via* gradient electrodeposition, which facilitates alloy development.

To study the electrochemical properties of different compositions, we present the cyclic voltammogram (CV) of S09, S41, and S73 and compared them with pure Ni foil in coin cells. Fig. 4a shows the typical CV curve of pure Ni foil between 0.01 V and 2.0 V. No current response excludes the existence of native nickel oxides, which contribute to the CV current and affect the analysis of alloys. As shown in Fig. 4b, the CV curves of the S09 anode exhibit the peak at ~0.80 V in the 1st lithiation, which is attributed to the lithiation of Sb [15,22]. The cathodic current peaks at 0.20–0.50 V can be assigned to the lithiation reactions of the Sn component in the alloys. Sn lithiation usually involves multiple steps and shows several peaks based on the literature [26–28]. It is noted that the Sn cathodic peak shifted to a higher potential in the 2nd and 3rd cycles probably because the lithiation and delithiation of pristine $SnCo_2$ and SnSb alloys in the first cycle reduce the annealed alloy grains to the smaller size. A small alloy grain needs relatively low activation energy for lithiation. The extra capacity between the 1st and 2nd results from the formation of a solid electrolyte interface (SEI) [29–31]. During the 1st delithiation, the CV peaks around ~0.8 V are ascribed to the delithiation process of Li_xSn. The oxidation peak at ~1.10 V is due to the delithiation of the Li_3Sb alloy [32,33]. These current-potential characteristics were in agreement with the previous reports on the electrodeposited Sn or Sb anodes [33,34].

For the S41 anode, the position of Sb peaks remains unchanged during lithiation/delithiation. The lithiation peak at 0.50 eV increases, and the delithiation peak at 0.80 eV decreases, indicative of better charge/discharge reversibility. In addition, it can be found that the area of oxidation and reduction peaks gradually decreases from S09, S41, to S73, which also reflects the trend of the charge/discharge capacity.

Galvanostatic charge/discharge tests were conducted for nine Sn–Co–Sb alloys with Li foil as the anodes. The large initial capacity and the capacity difference between the first two cycles indicate the formation of the SEI. As shown in Fig. 5, the S09 alloy shows two platforms in the discharge curves, corresponding to the formation of the Li–Sb alloy and a multistep lithiation of Sn, respectively. Two

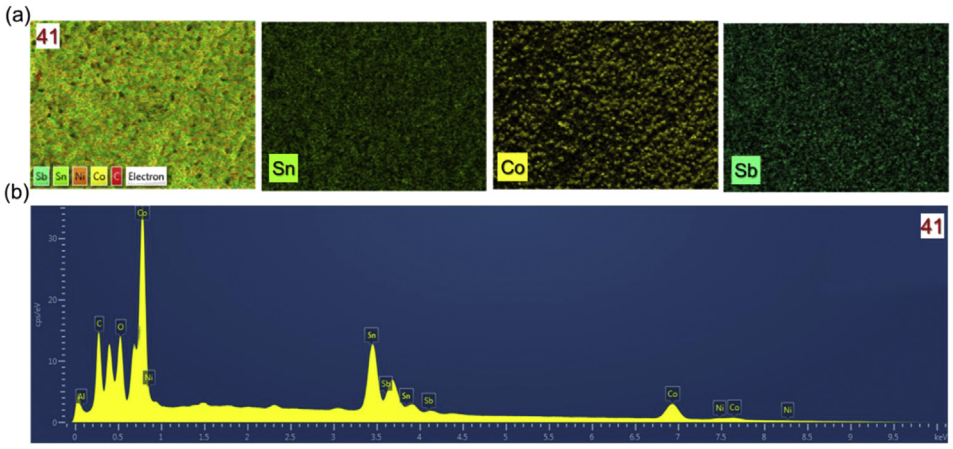

(c)

Sample	Sn (wt%)	Co (wt%)	Sb (wt%)
01	66.0	10.2	23.8
05	71.8	10.9	17.3
09	80.4	10.6	9.0
37	65.5	12.2	22.3
41	71.3	12.8	15.9
45	75.4	14.2	10.4
73	60.7	15.2	24.1
77	67.9	15.4	16.7
81	70.6	16.5	12.9

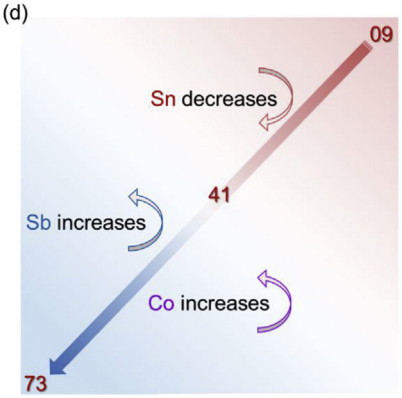

Fig. 3. (a) EDX mapping images and (b) spectrum of S41. (c) The elemental composition of samples. (d) Schematic diagram of the changes in the content of Sn, Co, and Sb in the Sn–Co–Sb alloy. EDX, energy-dispersive X-ray.

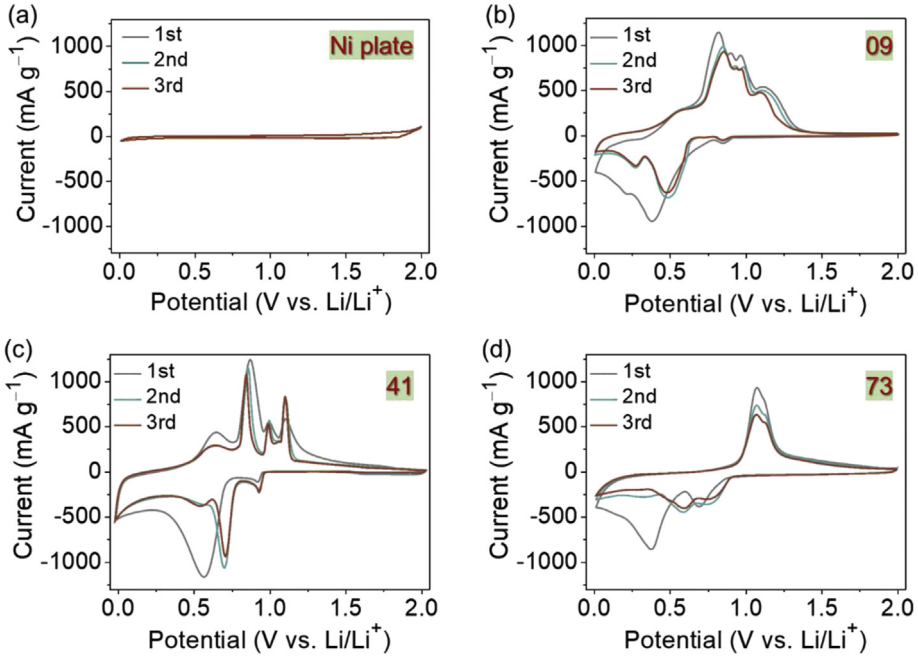

Fig. 4. Cyclic voltammetry curves of the (a) Ni flat anode, (b) S09 anode, (c) S41 anode, and (d) S73 anode.

platform potentials at ~0.8 and ~1.10 V in the charge curves are in agreement with the peaks of CV curves in Fig. 4b and attributed the delithiation of Li_xSn and Li_3Sb, respectively. The discharge/charge curves of Sn, Sb, and Co were also provided in Figs. S1–S3 for comparison. Each alloy electrode shows different discharge capacity, voltage platform, and polarization. By comparing the voltage curves of all nine alloys, the lithiation potential of the Sb reaction does not significantly change in these electrodes, whereas the

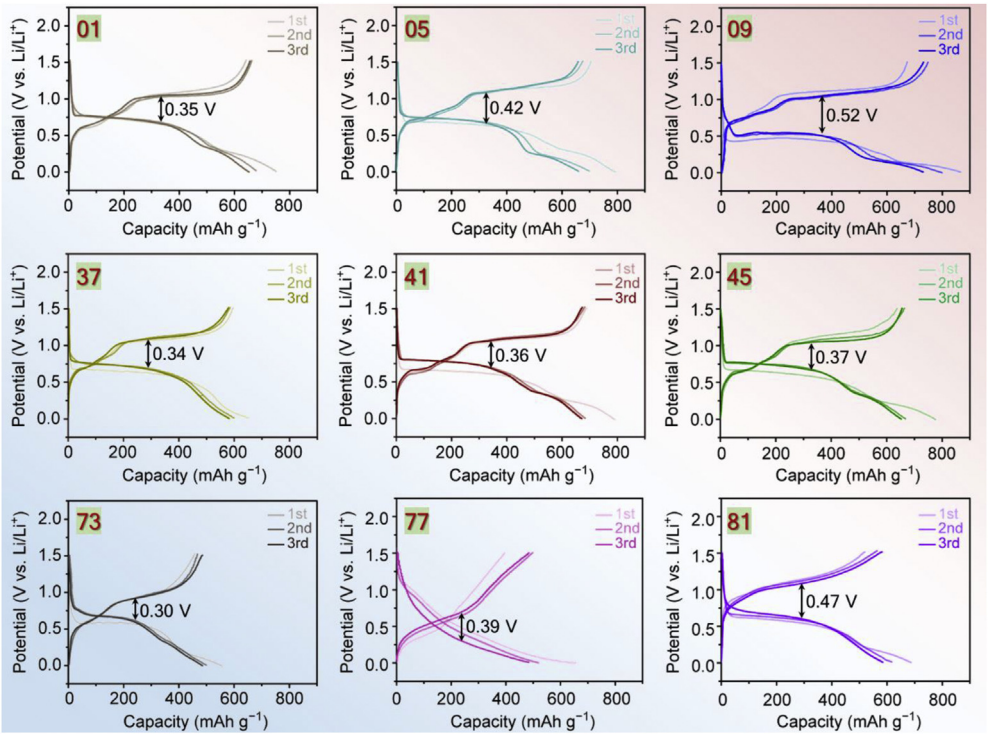

Fig. 5. Galvanostatic discharge/charge curves of the alloy electrodes.

lithiation potential of Sn reactions significantly changes. This potential shift can be attributed to the phase change of Sn in alloys.

The S09 alloy has the largest discharge capacity (733.8 mAh g^{-1}) among the nine samples mainly because of its highest Sn content. The S05, S41, and S45 alloys deliver similar discharge capacities of 662.4, 671.8, and 653.3 mAh g^{-1}, respectively. The decrease in capacity is mainly due to the low Sn content and high Sb content. The theoretical specific capacity of Sb is lower than that of Sn. Similarly, the lithiation capacity of the other samples decreases with the decrease of Sn and the increase of Co and Sb. Generally, in the diagonal direction from S09, S41, to S73, the lithiation capacity of alloys is gradually reduced. The S73 alloy has the smallest discharge capacity of 486.7 mAh g^{-1}.

Polarization is another important indicator to evaluate the electrode performance. As compared with S09, the S41 alloy exhibits a high lithiation voltage platform, indicating that it can reduce the polarization overpotential. A low polarization can improve the efficiency of energy conversion. An appropriate amount of Co and Sb lowers the polarization of S41 [35,36]. The S73 alloy also has a low polarization overpotential. However, its specific capacity was reduced by the low fraction of Sn. Thus, the overall comparison leads us to conclude that the S41 alloy has the best electrochemical properties because of its high capacity and low polarization overpotentials.

Fig. 6a presents the cycling properties of S09, S41, and S73. All the three alloys deliver a high capacity in the 1st cycle and low initial coulombic efficiencies (CEs) of ~80%. The low CEs in the first few cycles are usually related to SEI formation [27], which is consistent with the CV analysis. Upon cycling, the CEs increase rapidly to be more than 95% in only a few cycles. After the initial decrease of capacity in the first few cycles, these alloy electrodes seem to reach a stable state. The capacity of S09 can maintain around 603 mAh g^{-1} for about 120 cycles and then abruptly decreases to 58% of its initial capacity in the 200th cycle. The specific capacity of S41 remains almost constant at 620.2 mAh g^{-1} for 200 cycles, indicating the good cycling stability. The S73 alloy shows a capacity decay from 459.6 mAh g^{-1} to 385.8 mAh g^{-1} for 200 cycles. The dramatic difference of S09, S41, and S73 in cycling properties can be attributed to their electrode microstructure, phase composition, and the Sn:Co:Sb ratio. Sn provides high capacity but does not cycle well. Adding Co and Sb to Sn alloys may help to stabilize the cyclability of Sn alloys. However, the theoretical capacity of Sb is lower than that of Sn, and Co has no capacity (Figs. S1–S3); too much Sb and Co will significantly lower the alloy's capacity, and therefore, a constant amount of Sb and Co is adopted. Sb and Co can improve the interaction force between Sn atoms after forming an alloy with Sn, thereby improving the stability of the electrode [22]. Thus, a rational design of multi-elemental alloys is needed to optimize their composition *via* high-throughput fabrication and characterization.

To further study the degradation of alloys during cycling, electrochemical impedance spectroscopy (EIS) was conducted to monitor the impedance changes. Fig. 6b and c presents the Nyquist plots of S09, S41, and S73 in the 10th and 200th cycles from 100 kHz to 0.1 Hz. The EIS curves exhibit significantly depressed semicircles and straight lines. We use the equivalent circuit in Fig. 6c to fit the EIS spectra. The depressed semicircles are attributed to the overlap of multiple semicircles. During lithiation, alloys form the SEI, which contributes one semicircle at high frequencies. Another semicircle at medium frequencies is due to the charge transfer. The straight line at low frequencies is the typical characteristics of the Li-ion migration through electrodes [37,38]. Table 1 lists the fitted resistances of the electrolyte and/or contact (R_E), SEI (R_{SEI}), and charge transfer (R_{CT}). The S41 alloy shows a lower R_E and R_{CT} than S09 and S73, suggesting that S41 has a high electrical conductivity, which agrees with better rate capability and higher reversible capacity. After 200 cycles, the R_{SEI} of S41 increases by 17.7%, whereas that of S09 and S73 increases by 70.9% and 20.1%, respectively. The impedance increase of the SEI mainly leads to the capacity decay of these alloy electrodes during cycling.

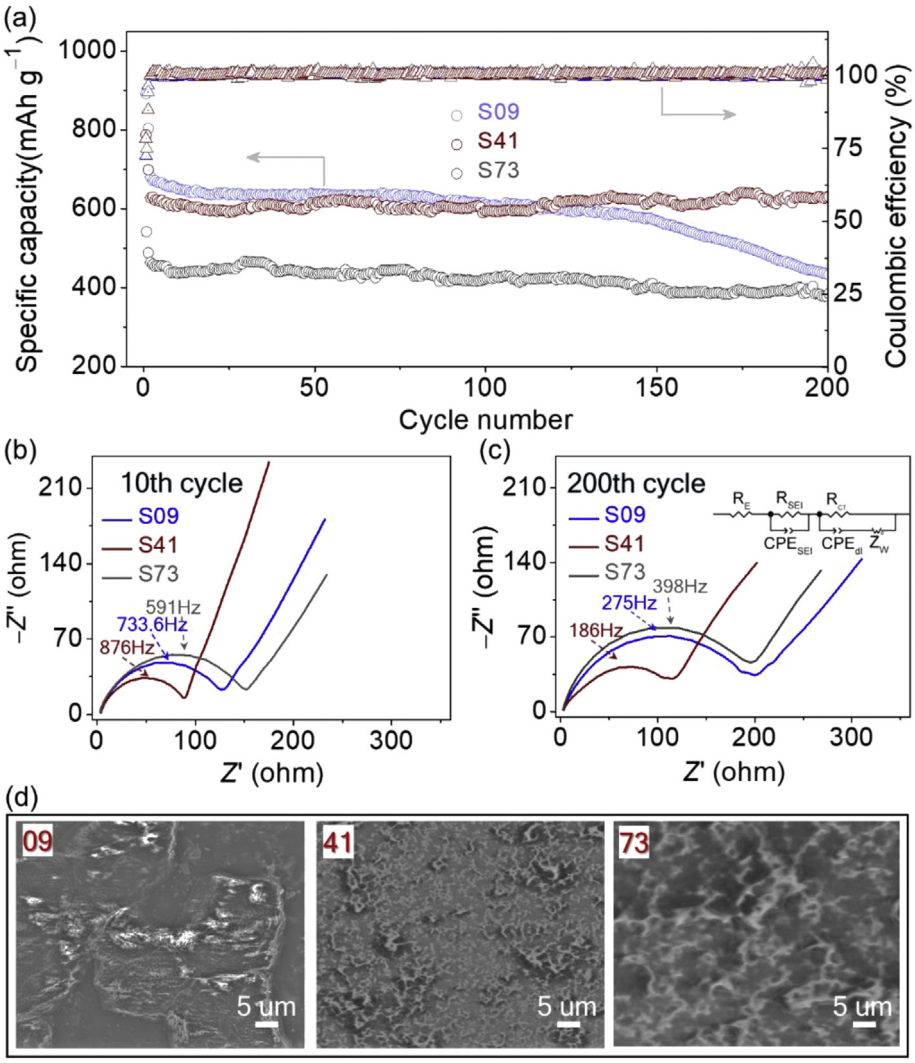

Fig. 6. (a) The long cycle performance of S09, S41, and S73 alloy electrodes at 0.2 A g^{-1}. Nyquist plots for of S09, S41, and S73 alloy electrodes for (b) 10th cycles and (c) 200th cycles. (d) SEM images of S09, S41, and S73 alloy electrodes after cycling 200 times. SEM, scanning electron microscopy.

The capacity decays are also related to the evolution of microarchitecture and structural stability of alloys during cycling. We disassembled the cycled S09, S41, and S73 alloy and observed their SEM images (Fig. 6d). After 200 cycles, the surface of all cycled alloys becomes rough as compared with electrodeposited alloys (Fig. 2). For the S09 alloy, the alloy deposit has been aggregated into large micron particles. Some parts are delaminated from Ni foil probably because the high Sn content in S09 leads to a large volume change, and the accumulated stress detaches the deposit from Ni foil [23,39]. The incrementally increased SEI in the crack may kinetically isolate the cracked alloy particles, leading to rapid capacity decay. The S41 alloy forms a continuous and fine conductive network on the surface, which helps to support and accommodate the multistep volume changes. The increased Co and Sb components in S41 can buffer the volume change during the alloying process of Sn [22,40–42], leading to the high reversible lithium storage capacity and good cycling stability. The S73 alloy shows a larger conductive network, and however, its capacity is low because of low Sn content. Therefore, through rapid gradient screening, we are able to obtain an optimal Sn–Co–Sb alloy (S41 alloy) ratio, which exhibits the favorable microstructures for cycling and demonstrates the best electrochemical properties. Furthermore, we fabricated a large Sn–Co–Sb alloy with a similar Sn:Co:Sb ratio as S41 (as shown in Figs. S4 and S5) by keeping the two electrodes parallel to each other during the electrodeposition process and adjusting the electroplating current and time of different metals. Subsequently, we randomly cut an electrode sample with a size of 1 cm × 1 cm from the enlarged alloy electrode as the anode electrode of coin cells for testing. Fig. S6 presents the cycling properties of the selected sample. It can be seen that the selected sample shows similar discharge capacity and cyclic stability to S41 in Fig. 6a. It indicates that the optimal alloy composition obtained by rapid screening can also show good performance after scale-up.

Table 1
The fitted R_E, R_{SEI}, and R_{CT}.

Electrodes	10th cycle			200th cycle		
	R_E (Ω)	R_{SEI} (Ω)	R_{CT} (Ω)	R_E (Ω)	R_{SEI} (Ω)	R_{CT} (Ω)
S09	1.33	71.29	54.09	2.29	121.90	78.53
S41	1.63	52.45	34.36	2.00	61.75	49.27
S73	1.75	95.67	50.82	1.95	114.90	75.59

Table 2
The electrodeposition parameters for Sn, Co, and Sb layers on the Ni flat.

Angle	Electrodeposition	Plating solution	Work electrode	Counter electrode	Plating current
0°	Sn layer	$SnCl_2{\cdot}2H_2O/K_4P_2O_7$/glycine/$C_4O_6H_4KNa$	Ni flat	Sn foil	−6.25 mA cm^{-2} (1 s on, 10 s off)
90°	Co layer	$CoSO_4{\cdot}6H_2O/H_3BO_3$ $Co_2Cl_2{\cdot}6H_2O$	Ni@Sn	Ni flat	−2 mA cm^{-2}
180°	Sb layer	$SbCl_3$/glycine/$C_4O_6H_4KNa$	Ni@SnCo	Pt flat	−6.25 mA cm^{-2} (1 s on, 10 s off)
270°	Sn layer	$SnCl_2{\cdot}2H_2O/K_4P_2O_7$/glycine/$C_4O_6H_4KNa$	Ni@SnCoSb	Sn foil	−6.25 mA cm^{-2} (1 s on, 10 s off)

3. Conclusion

In summary, a gradient electrodeposition technology was developed to enable a high-throughput fabrication of alloy anodes. We demonstrated the effectiveness of gradient electrodeposition in the development of Sn−Co−Sb alloy anodes. The gradient distributions of Sn, Co, and Sb in one large sample were realized by tilting and alternatively rotating the working electrode contents. The following heat treatment produces varied compositions in the different regions of the sample, which can be further cut to 9 × 9 smaller samples for characterization. Such a rapid fabrication allows us to optimize the Sn−Co−Sb alloy anode for high-energy Li-ion batteries. After microstructural and electrochemical analyses, we found that the Sn:Co:Sb mass ratio of 71.3:12.8:15.9 (wt%) shows a high reversible capacity of 671.8 mAh g^{-1} and good cycling properties for more than 200 cycles. The excellent electrochemical performance can be attributed to the optimized Sn:Co:Sb ratio and microstructure. An appropriate Sn content provides a high capacity without sacrificing cyclability because Co and Sb can buffer the large volume change, thereby leading to the high reversible lithium storage capacity and good cycling stability. This study demonstrates that the gradient electrodeposition-based high-throughput fabrication method can quickly search parameter space of elemental composition and screen out the best Sn−Co−Sb alloy anode for Li-ion batteries. More important, the gradient electrodeposition is a general method and can be extended to other alloys systems for Li-ion and Na-ion battery anodes.

4. Experimental section

4.1. Raw materials

NaOH and H_2SO_4 (analytical grade) were obtained from Nanjing Chemical Reagent Co., Ltd. $SnCl_2{\cdot}2H_2O$, $K_4P_2O_7$, glycine, $C_4O_6H_4KNa$, $CoCl_2{\cdot}6H_2O$, $CoSO_4{\cdot}6H_2O$, H_3BO_3, and $SbCl_3$ (analytical grade) were bought from Shanghai Sinopharm Chemical Reagent Co., Ltd. Ni flat (thickness: 0.1 mm), Pt flat (thickness: 0.1 mm), and Sn foil (thickness: 0.025 mm) were also provided by Sigma-Aldrich Corp.

4.2. Preparation of Sn−Co−Sb alloys

Sn−Co−Sb alloys were synthesized by sequentially plating Sn, Co, Sb, and Sn on a Ni foil, which was tilted 15° from the counter electrodes. The gradient electrodeposition differs from the conventional parallel alignment of working and counter electrodes. The electrodeposition parameters are shown in Table 2. The plating solution for Sn contained 0.088 M $SnCl_2{\cdot}2H_2O$, 0.909 M $K_4P_2O_7$, 0.107 M glycine, and 0.028 M $C_4O_6H_4KNa$. The plating current pulse was −6.25 mA cm^{-2} (1 s on and 10 s off). After Sn electrodeposition, the resultant Ni@Sn sample was rinsed with deionized water, rotated 90°, and immersed in a plating solution of 0.088 M $CoCl_2{\cdot}6H_2O$, 0.088 M $CoSO_4{\cdot}6H_2O$, and 0.088 M H_3BO_3 to electrodeposit Co. A galvanostatic current of −2 mA cm^{-2} was applied. After Co electrodeposition, the obtained Ni@SnCo sample was rinsed with deionized water and rotated 90°again for Sb electrodeposition. The Sb plating solution is composed of 0.035 M $SbCl_3$, 0.9 M $K_4P_2O_7$, 0.1 M glycine, and 0.028 M $C_4O_6H_4KNa$. The counter electrodes were Pt flat. The plating current pulses were −6.25 mA cm^{-2} (1 s on and 10 s off). After cleaning and rotation, Sn was electrodeposited on the resulting sample using the same plating method as the first step. The obtained Ni@SnCoSbSn sample was annealed at 300 °C for 2 h in Ar gas to obtain the Sn−Co−Sb alloy electrodes. The composition of Sn, Co, and Sb could be tuned by pulse number and pulse duration. The relative loading ratio was adjusted by varying the plating time and current as per the demanded energy or power density of batteries. The Sn−Co−Sb loading was controlled ~2 mg cm^{-2}. The Sn−Co−Sb alloy electrode was evenly cut into 81 pieces for further characterization.

4.3. Material and electrochemical characterizations

The XRD patterns were collected using a Rigaku D/MAX2500 V with Cu Kα radiation (λ = 1.5418 Å). The SEM morphologic and EDX mapping images were obtained using a field-emission scanning electron microscope (Zeiss Ultra 55). The electrochemical performances of Sn−Co−Sb alloys were investigated by assembling coin-type cells with Li foil as a counter electrode in a purified argon-filled glove box. The electrolyte for the cell was 1.0 M $LiPF_6$ solution in 1:1:1 (volume ratio) mixture of ethylene carbonate, ethyl methyl carbonate solution, and dimethyl carbonate. Before all electrochemical tests, the cells were kept at room temperature for 24 h. Galvanostatic charge and discharge were carried out between 0.01 V and 2 V using a Land Battery Tester (CT2001A). CVs were measured using a VSP potentiostat (Bio-Logic Corp.).

CRediT authorship contribution statement

C. Zhong: Resources, Investigation, Methodology, Writing - original draft, Writing - review & editing. **C. Guo:** Investigation, Methodology, Writing - original draft. **X. Jin:** Methodology, Visualization. **Y. Li:** Investigation. **J. Chen:** Investigation. **S. Zhang:** Methodology, Investigation. **Y. Lu:** Methodology. **H. Zhang:** Resources, Methodology, Supervision, Writing - review & editing. **F. Pan:** Resources, Methodology, Supervision, Writing - review & editing.

Declaration of Competing Interest

The authors declare that they have no known competing financial interests or personal relationships that could have appeared to influence the work reported in this paper.

Acknowledgments

The authors acknowledge the financial support of the National Key R&D Program of China (2016YFB0700600) and the National Natural Science Foundation of China (21776121).

Appendix A. Supplementary data

Supplementary data to this article can be found online at https://doi.org/10.1016/j.mtener.2020.100528.

References

[1] F. Sun, H.B. Wu, X. Liu, F. Liu, R. Han, Z.B. Qu, X.X. Pi, L.J. Wang, J.H. Gao, Y.F. Lu, Mater. Today Energy 9 (2018) 428–439.
[2] P.K. Nayak, L.T. Yang, W. Brehm, P. Adelhelm, Angew. Chem. Int. Ed. 57 (2018) 102–120.
[3] N. Nitta, F. Wu, J.T. Lee, G. Yushin, Mater. Today 18 (2015) 252–264.
[4] B. Cao, X.F. Li, Acta Phys. - Chim. Sin. 36 (2020) 16.
[5] B. Wang, T.T. Ruan, Y. Chen, F. Jin, L. Peng, Y. Zhou, D.L. Wang, S.X. Dou, Energy Storage Mater. 24 (2020) 22–51.
[6] L.B. Ni, G. Yang, C.Y. Sun, G.S. Niu, Z. Wu, C. Chen, X.X. Gong, C.Q. Zhou, G.J. Zhao, J. Gu, W. Ji, X. Huo, M. Chen, G.W. Diao, Mater. Today Energy 6 (2017) 53–64.
[7] J. Zhou, Z. Jiang, S. Niu, S. Zhu, J. Zhou, Y. Zhu, J. Liang, D. Han, K. Xu, L. Zhu, X. Liu, G. Wang, Y. Qian, Inside Chem. 4 (2018) 372–385.
[8] S.F. Liu, X.H. Xia, Y. Zhong, S.J. Deng, Z.J. Yao, L.Y. Zhang, X.-B. Cheng, X.L. Wang, Q. Zhang, J.P. Tu, Adv. Energy Mater. 8 (2018) 1702322.
[9] M. Li, H.R. Du, L. Kuai, K.F. Huang, Y.Y. Xia, B.Y. Geng, Angew. Chem. Int. Ed. 56 (2017) 12649–12653.
[10] A. Nurpeissova, A. Adi, A. Aishova, A. Mukanova, S.S. Kim, Z. Bakenov, Mater. Today Energy 16 (2020) 100397.
[11] H. Peng, R. Li, J. Hu, W. Deng, F. Pan, ACS Appl. Mater. Interfaces 8 (2016) 12221–12227.
[12] J. Yang, M. Winter, J.O. Besenhard, Solid State Ionics 90 (1996) 281–287.
[13] J. Hassoun, G. Derrien, S. Panero, B. Scrosati, Electrochim. Acta 54 (2009) 4441–4444.
[14] F.S. Ke, L. Huang, H.-B. Wei, J.S. Cai, X.-Y. Fan, F.Z. Yang, S.G. Sun, J. Power Sources 170 (2007) 450–455.
[15] S. Wang, P.K. Lee, X.M. Yang, A.L. Rogach, A.R. Armstrong, D.Y.W. Yu, Mater. Today Energy 9 (2018) 295–302.
[16] J. Hassoun, S. Panero, P. Simon, P.L. Taberna, B. Scrosati, Adv. Mater. 19 (2007) 1632–1635.
[17] F.S. Ke, L. Huang, J.S. Cai, S.G. Sun, Electrochim. Acta 52 (2007) 6741–6747.
[18] W. Liu, J. Zhang, Z. Bai, G. Jiang, M. Li, K. Feng, L. Yang, Y. Ding, T. Yu, Z. Chen, A. Yu, Adv. Funct. Mater. 28 (2018) 1706675.
[19] H. Kim, J. Cho, Electrochim. Acta 52 (2007) 4197–4201.
[20] H.K. Wang, Q.Z. Wu, D.X. Cao, X. Lu, J.K. Wang, M.K.H. Leung, S.D. Cheng, L. Lu, C.M. Niu, Mater. Today Energy 1–2 (2016) 24–32.
[21] R.M. Gnanamuthu, C.W. Lee, Mater. Sci. Eng., B 176 (2011) 1329–1332.
[22] S. Sengupta, A. Patra, M. Akhtar, K. Das, S.B. Majumder, S. Das, J. Alloys Compd. 705 (2017) 290–300.
[23] H. Zhang, T. Shi, D.J. Wetzel, R.G. Nuzzo, P.V. Braun, Adv. Mater. 28 (2016) 742–747.
[24] H. Yan, Y. Xie, A. Wu, Z. Cai, L. Wang, C. Tian, X. Zhang, H. Fu, Adv. Mater. 31 (2019) 1901174.
[25] X.Y. Fan, Y.X. Shi, J.J. Wang, J. Wang, L. Xu, L. Gou, D.L. Li, Ionics 19 (2013) 1551–1558.
[26] X. Zhou, J. Bao, Z. Dai, Y.G. Guo, J. Phys. Chem. 117 (2013) 25367–25373.
[27] L. Xue, X. Xia, T. Tucker, K. Fu, S. Zhang, S. Li, X. Zhang, J. Mater. Chem. A 1 (2013) 13807.
[28] W. Li, R. Yang, J. Zheng, X. Li, Nano Energy 2 (2013) 1314–1321.
[29] S. Rao, X. Zou, S. Wang, T. Shi, Y. Lu, L. Ji, H.-Y. Hsu, Q. Xu, X. Lu, J. Electrochem. Soc. 166 (2019) D427–D434.
[30] Y. Zhao, L. Yang, D. Liu, J. Hu, L. Han, Z. Wang, F. Pan, ACS Appl. Mater. Interfaces 10 (2018) 1672–1677.
[31] J.C. Li, J. Pu, Z.Q. Liu, J. Wang, W.L. Wu, H.G. Zhang, H.X. Ma, ACS Appl. Mater. Interfaces 9 (2017) 25250–25256.
[32] S. Fan, T. Sun, X. Rui, Q. Yan, H.H. Hng, J. Power Sources 201 (2012) 288–293.
[33] X. Chen, Q. Ru, D. Zhao, Y. Mo, S. Hu, J. Alloys Compd. 646 (2015) 794–802.
[34] F. Zhan, H. Zhang, Y. Qi, J. Wang, N. Du, D. Yang, J. Alloys Compd. 570 (2013) 119–124.
[35] S. Javadian, J. Kakemam, H. Gharibi, H. Kashani, Int. J. Hydrogen Energy 42 (2017) 13136–13149.
[36] A. Darwiche, C. Marino, M.T. Sougrati, B. Fraisse, L. Stievano, L. Monconduit, J. Am. Chem. Soc. 134 (2012) 20805–20811.
[37] Y. Zhao, X. Jin, Y. Lu, J. Pu, Z. Shen, C. Zhong, S. Zhang, J. Liu, H. Zhang, ChemElectroChem 7 (2020) 2026.
[38] S. Sengupta, A. Mitra, P.P. Dahiya, A. Kumar, M. Mallik, K. Das, S.B. Majumder, S. Das, J. Alloys Compd. 721 (2017) 236–248.
[39] K. Nishikawa, K. Dokko, K. Kinoshita, S.W. Woo, K. Kanamura, J. Power Sources 189 (2009) 726–729.
[40] G. Wang, Z.W. Lu, X.P. Gao, X.J. Liu, J.Q. Wang, J. Power Sources 189 (2009) 655–659.
[41] X.Y. Fan, F.S. Ke, G.Z. Wei, L. Huang, S.G. Sun, J. Alloys Compd. 476 (2009) 70–73.
[42] H. Gul, M. Uysal, T. Çetinkaya, M.O. Guler, A. Alp, H. Akbulut, Int. J. Hydrogen Energy 39 (2014) 21414–21419.